

Detection and characterization of large- and very large-scale motions in numerically simulated atmospheric boundary layer flows

Mohammad A. Khan · Rob Stoll

Received: DD Month YEAR / Accepted: DD Month YEAR

Abstract Previous studies confirmed the presence of Very Large Scale Motions (VLSMs) in channel and ABL flows through experimentation and simulations. However, due to limitations in experimentation and the lack of the account of Coriolis force in numerical simulations, the effects of rotation on VLSM have not been thoroughly examined. Here, the Large Eddy Simulation technique was used to simulate VLSMs under different degrees of rotation. Both traditional statistical and image processing techniques were then used to characterize them. The traditional method of determination of length scales of VLSMs from per-multiplied spectra of the stream-wise velocity component proved to be inadequate when rotation was introduced. By identifying the footprints of VLSMs as connected regions of low momentum fluid and then identifying those regions through standard image processing tools, the difficulties in determining the VLSM length scales could be circumvented. It was found that rotation inhibited the coherence and suppressed the development of VLSMs in the ABL flows. Also, it was found that the usual practice of visually identifying VLSM on numerically filtered velocity fields as long regions of low momentum might not be sufficiently accurate.

1 Introduction

In general, turbulent flows are composed of constituent coherent structures and background flows (Hussain, 1986) and the dynamics of these structures are considered fundamental to the understanding of mixing processes in the atmospheric boundary layer (ABL) (Fiedler, 1988; Lewalle et al., 2000). Recently the largest of these coherent motions termed very large scale motions (VLSMs) have garnered increased interests (e.g. Jacob and Anderson, 2017;

Mohammad A. Khan
first address
Tel.: +1-701-5407414
E-mail: ahsan.khan@utah.edu

Rob Stoll
Department of Mechanical Engineering
The University of Utah
Tel.: +1 801 581 3405
Fax: +1 801 585 5261
E-mail: rstoll@eng.utah.edu

Kerhervé et al., 2017). VLSMs are identified as very long regions of low-momentum fluid aligned in the streamwise direction that are flanked by high-momentum regions and they have been observed in turbulent pipe (Guala et al., 2006; Kim and Adrian, 1999; Monty et al., 2007), channel (Guala et al., 2006; Lee et al., 2014; Monty et al., 2007) and boundary layer flows (Fang and Porté-Agel, 2015; Hutchins and Marusic, 2007). The spatial length scale of VLSMs scales with δ , where δ refers to boundary layer (BL) height, channel half width or pipe radius (Chung and McKeon, 2010; Monty et al., 2007) and from flow visualizations, the largest length scale of VLSMs was shown to be approximately 20δ . However, a concrete definition of VLSMs is lacking which makes the identification of these structures highly subjective. From two-point correlation, the length scale is consistently under predicted and was reported to vary from 2.5δ to 4δ in the outer region of the BL. Spanwise meandering of VLSMs is one possible explanation for the underestimation of streamwise length scales from two-point correlations of streamwise velocity (Hutchins and Marusic, 2007). Furthermore, visual detection procedures that have been used are subjective in nature requiring the specification of a threshold value to visualize low-momentum or high-momentum regions. Dennis and Nickels (2011) appropriately pointed out that choosing a higher threshold may result in underestimation of the length of VLSMs, while inappropriate filtering may smooth away small-scale features and join them to give an impression of a single large-scale structure. A more objective definition or detection criteria of the length scales of VLSMs comes from premultiplied 1D spectra of the streamwise-velocity component. A bimodal distribution of energy is observed in the premultiplied spectra, where the low wavenumber peak corresponds to VLSMs and the most energy containing wavenumber mode before a sharp fall-off which corresponds to large-scale motions (LSMs). This observation of the bimodal distribution has been used to distinguish the two length scales i.e. LSM and VLSM (Balakumar and Adrian, 2007; Guala et al., 2006; Kim and Adrian, 1999). However, this scale identification from 1D spectra is not devoid of pitfalls. Hutchins and Marusic (2007) pointed out that the meandering nature of the VLSM can cause a shift of the energy peak in premultiplied spectra to shorter wavelengths. Also the approach of extracting a dominant wavelength from energy spectra of the streamwise velocity component to identify VLSMs has an inherent assumption (Baltzer et al., 2013) that spatially a low-momentum region would be in immediate vicinity of a high-momentum region of similar length scale in the streamwise direction, and since a VLSM structure represents only a half cycle of a sinusoidal function, the low wavenumber peak in spectra would be indicative of twice the length scale of the VLSM. These issues have resulted in discrepancies in the reported length scales of VLSMs from the premultiplied spectra and visualization methods. In logarithmic regions of channel and boundary layer flows energy peaks corresponding to wavelengths 7.5δ and 5δ has been reported (Balakumar and Adrian, 2007), whereas VLSM length scales of the order of 10δ have been reported from visualizations in both cases (Hutchins and Marusic, 2007; Lee et al., 2014; Lee and Sung, 2011) giving rise to the need for alternative approaches to assess the importance of VLSMs and identifying their length scale.

The rich features of VLSMs and their importance were demonstrated in both experimental (Guala et al., 2006; Hutchins and Marusic, 2007; Kim and Adrian, 1999; Monty et al., 2007) and numerical studies (Fang and Porté-Agel, 2015; Lee et al., 2014; Lee and Sung, 2011). The importance is manifest in their contribution to the overall magnitude of Reynold's stress and turbulent kinetic energy. In pipe flow cumulative distribution of turbulent kinetic energy and Reynold's stress over Fourier modes revealed that more than 65% of turbulent energy was due to VLSMs, while their contribution to Reynold's shear stress accounted as much as 60% (Guala et al., 2006). It was also found that large scale motions with an estimated eddy turn over time of $2\delta/U_\infty$ (where U_∞ denotes the free streamwise velocity) or

greater strongly modulate the magnitude of smaller scale fluctuations within the log region and they modulate the frequency of small-scale fluctuations even more above the log region (Ganapathisubramani et al., 2012).

Here, our focus is the characterization of VLSMs in the ABL and how they are impacted by the Coriolis force. Unlike small-scale laboratory flows, the effect of the Earth's rotation can not be ignored in the ABL, therefore, to faithfully represent ABL physics, conservation equations must be studied in a rotational frame of reference. When conservation of momentum is expressed in a rotational frame, the Earth's rotation is accounted for by introduction of the Coriolis force which can have an impact on the size and shape of the large eddies in the flow field (Esau, 2003). Although, the Coriolis force does not contribute to the velocity magnitude, mean kinetic energy or turbulent kinetic energy (*tke*), its importance in kinetic energy redistribution among different scales can be identified in low Rossby number (Ro) flows (Hossain, 1994; Yeung and Zhou, 1998). In the limiting case of $Ro = 0$, i.e., in case of solid body rotation or low enough Ro number where inertia is negligible compared to the Coriolis force, Taylor Proudman column vortices appear as a result of the dimensional reduction. So, It can intuitively be predicted that Coriolis force can have an impact on large-scale coherent structures, although, the effect is not readily comprehensible.

The main objective of this study is to discern the effect of rotation on the characteristics of VLSMs. Large-eddy simulations (LES) were carried out over large domains to simulate the Earth's rotational effect. We focused on the coherence of the flow and looked into the known signatures of VLSMs to understand how rotation impacts their characteristics. The quantitative aspect of the contribution of VLSMs under the effect of rotation in Reynold's stresses was studied. A relatively straight forward definition of VLSMs was developed to facilitate a VLSM detection method based on widely used image processing techniques.

2 Numerical Simulation

In this study, LES was used to examine the effect of rotation on VLSMs. The models and numerics used in the simulation code are described in detail in Stoll and Porté-Agel (2006) and Stoll and Porté-Agel (2008). Here only a brief summary is given. The numerical code solves the spatially filtered incompressible Navier-Stokes equations in rotational form,

$$\frac{\partial \tilde{u}_i}{\partial t} + \tilde{u}_j \left(\frac{\partial \tilde{u}_i}{\partial x_j} - \frac{\partial \tilde{u}_j}{\partial x_i} \right) = -\frac{\partial \tilde{p}^*}{\partial x_i} - \frac{\partial \tau_{ij}}{\partial x_j} + f_c \epsilon_{ij3} \tilde{u}_j, \quad (1)$$

where \tilde{u}_i denotes the spatially-filtered, resolved velocity in the i -th direction, x_i is the spatial coordinate and $i = 1, 2, 3$ corresponds to the streamwise, spanwise, and surface normal directions, respectively. $p^* = p' / \rho + \frac{1}{2} \tilde{u}_i \tilde{u}_i$ is the modified pressure, τ_{ij} is the sub-grid scale (SGS) stress tensor, f_c is the Coriolis parameter, and ϵ_{ijk} is the permutation tensor. Viscous forces were assumed to be negligible as a result of the extremely high-Reynolds number of the ABL and τ_{ij} was computed using the scale dependent Lagrangian-averaged dynamic Smagorinsky model of Stoll and Porté-Agel (2006). Horizontal derivatives were calculated using a pseudo-spectral method, while vertical derivatives were approximated using second-order central differences, and for time integration the second-order Adams-Bashforth scheme was used. As surface boundary conditions, the required instantaneous surface shear stresses $\tau_{i3,s}(x, y, t)$ were computed from the instantaneous filtered velocity field at the lowest vertical grid level by local application of Monin-Obukhov similarity theory (Stoll and Porté-Agel,

2006) as,

$$\tau_{i3,s}(x, y, t) = - \left[\frac{\tilde{u}_r(x, y, (\Delta z/2), t) \kappa}{\ln((\Delta z/2)/z_o)} \right]^2 \frac{\tilde{u}_i(x, y, (\Delta z/2), t)}{\tilde{u}_r(x, y, (\Delta z/2), t)}, \quad (2)$$

where κ is the von karman constant ($= 0.4$), z_o is the local aerodynamic roughness ($= 0.1\text{m}$ in all simulated cases), $\tilde{u}_r(x, y, \Delta z/2, t) = [\tilde{u}_1(x, y, \Delta z/2, t)^2 + \tilde{u}_2(x, y, \Delta z/2, t)^2]^{1/2}$ is the local horizontal wind speed and Δz is the numerical grid spacing in the vertical direction. Although application of Monin-Obukhov similarity theory is not strictly valid instantaneously and locally, sensitivity tests indicate that its primary impact on the flow dynamics is confined to the lowest computational levels (Stoll and Porté-Agel, 2006). This numerical code has been used to simulate the ABL under a variety of different conditions (e.g., Bailey and Stoll, 2013; Miller and Stoll, 2013; Stoll and Porté-Agel, 2009) and to examine the structure and evolution of turbulent motions (e.g., Bailey and Stoll, 2016; Bailey et al., 2014). Its excellent representation of SGS momentum fluxes (Stoll and Porté-Agel, 2006) makes it ideal for an examination of large-scale ABL velocity field dynamics.

2.1 Simulation Setup

Three different simulated flow cases were examined to assess the effect of rotation on the characteristics of VLSMs in the ABL. Each case was characterized by a different Ro with the limiting infinite Ro case being a classical channel flow simulation under neutral stability condition driven by a constant horizontal pressure gradient ($CHNL$), and two Ekman layer simulation cases $EK10$ and $EK02$ with different degrees of rotation.

The focus of the study is large scale dynamics, and therefore, the simulation domain spans large horizontal extents in the x_1 ($L_1 = 128 \text{ Km}$) and x_2 ($L_2 = 128 \text{ Km}$) directions and has a height of 1500 m (L_3) for $CHNL$ and $EK10$ and a height of 750 m for $EK02$ in the vertical direction. The corresponding numerical grid is discretized with $N_1 = 2048$, $N_2 = 2048$ and $N_3 = 64$ nodes. A summary of the discretization along with basic parameters of the simulations are furnished in table 1, where u_* denotes the friction velocity, U_g denotes the geostrophic wind velocity in the x_1 -direction, δ stands for the boundary layer height, and Ro signifies the importance of rotation in the flow field defined as $Ro = U(2\Omega L)^{-1}$, where U is the characteristic flow velocity associated with the integral length scale L , Ω is the reference frame rate of rotation. For the $CHNL$ case the flow is driven by a constant mean pressure gradient along the streamwise direction with a prescribed value of $\langle \rho^{-1} \frac{\partial \bar{p}}{\partial x_1} \rangle = 1.3419 \times 10^{-9} \text{ ms}^{-2}$ where $\langle \rangle$ denotes a horizontal mean. The assumed balance between pressure and Coriolis force ($\langle \rho^{-1} \frac{\partial \bar{p}}{\partial x_i} \rangle = f_c \epsilon_{ij3} \tilde{u}_j$) and the imposed stress free condition ($\frac{\partial \tilde{u}_1}{\partial x_3} = \frac{\partial \tilde{u}_2}{\partial x_3} = 0$) at the domain top boundary result in the formation of an Ekman layer. The $EK10$ case mirrors the simulations of Andren et al. (1994) except for the facts that the domain is much larger in the horizontal directions and the vertical component of the Coriolis force is absent. In terms of forcing the difference between the simulated $CHNL$ and Ekman layer cases is that, in $CHNL$ constant pressure gradients $\langle \rho^{-1} \frac{\partial \bar{p}}{\partial x_1} \rangle$ acts on the flow while in $EK10$ and $EK02$ constant $\langle \rho^{-1} \frac{\partial P}{\partial x_1} \rangle = -f_c (\langle u_2 \rangle - V_g)$, and $\langle \rho^{-1} \frac{\partial P}{\partial x_2} \rangle = f_c (\langle u_1 \rangle - U_g)$ are forcing the flows.

Precursor simulations were carried out to generate initial flow fields for $EK10$ and $EK02$ using a one-dimensional single column model following the initialization procedure of An-

dren et al. (1994). Prognostic equations for the precursor simulations of *EK10* and *EK02* where

$$\begin{aligned}\frac{\partial \langle u_1 \rangle}{\partial t} &= f(\langle u_2 \rangle - V_g) - \frac{\partial}{\partial x_3} \langle u'_1 u'_3 \rangle \quad \text{and} \\ \frac{\partial \langle u_2 \rangle}{\partial t} &= f(\langle u_1 \rangle - U_g) - \frac{\partial}{\partial x_3} \langle u'_2 u'_3 \rangle.\end{aligned}\quad (3)$$

The turbulent stresses in Eqn. 3 $\langle u'_1 u'_3 \rangle$ and $\langle u'_2 u'_3 \rangle$ are estimated using eddy diffusivity models with $\langle u'_1 u'_3 \rangle = -k_m^u \frac{\partial \langle u \rangle}{\partial x_3}$ and $\langle u'_2 u'_3 \rangle = -k_m^v \frac{\partial \langle v \rangle}{\partial x_3}$. Eddy diffusivities in turn were approximated using a mixing length model, i.e., $k_m^u = l_m^2 \frac{\partial \langle u \rangle}{\partial x_3} f_m$ and $k_m^v = l_m^2 \frac{\partial \langle v \rangle}{\partial x_3} f_m$, where l_m is a mixing length estimated to match the initial profiles of Andren et al. (1994) and f_m is a prescribed correction factor. The time integration used a second order Adams-Bashforth model and was run until quasi-equilibrium. The LES 3D initial velocity fields were generated by adding random fluctuations to the mean vertical profiles in the surface layer.

3 Results

Analysis of the simulation output started with integrated and planar velocity field statistics to establish the convergence of the simulations and elucidate the primary differences in the mean flow fields. Next, planar linear correlations in the velocity field were also studied to examine the coherence of the flow before proceeding to the direct identification and characterization of VLSMs.

3.1 Bulk Statistics and Mean Vertical Profiles

The level of non-stationarity in the mean velocity fields can be measured in terms of coefficients C_u and C_v where,

$$\begin{aligned}C_u &= -\frac{f}{\langle u'_1 u'_3 \rangle_0} \int_0^{x_3^{top}} (\langle \bar{u}_2 \rangle - V_g) dx_3 \quad \text{and} \\ C_v &= \frac{f}{\langle u'_1 u'_3 \rangle_0} \int_0^{x_3^{top}} (\langle \bar{u}_1 \rangle - U_g) dx_3.\end{aligned}\quad (4)$$

For a horizontally homogeneous turbulent flow field C_u and C_v have steady-state values of unity (Garraat, 1992). Unsteadiness in C_u and C_v with respect to the non-dimensional inertial time tf are shown in Fig. 1(a). Increased non-stationarity is observed in *EK10* compared to *EK02* especially in the C_v values. Although, the oscillations in the two cases tend to have similar damping a discernible phase lag can be detected. The oscillations are expected to diminish exponentially around the $C_u, C_v = 1$ line (Garraat, 1992). Compared to Andren et al. (1994), in the *EK10* case the amplitude of the oscillations is smaller, a result of averaging the velocities over a larger domain. Overall, the oscillations behave as expected and the simulations are reasonably converged.

The nondimensional streamwise velocity gradient, $\Phi_M = \kappa x_3 u_*^{-1} d \langle \bar{u}_1 \rangle / dx_3$, where $u_* = -(\langle (\tau_{13,s})^2 + (\tau_{23,s})^2 \rangle)^{1/4}$ is plotted against nondimensional height in Fig. 1(b). Following similarity theory, Φ_M can be predicted to have a value of approximately unity in the

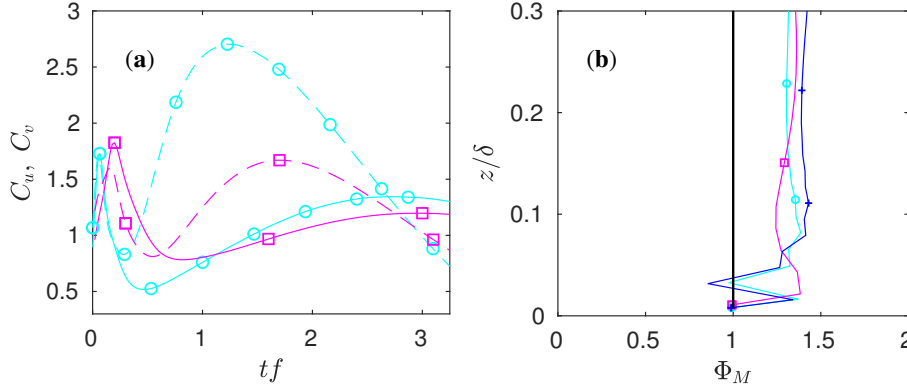


Fig. 1 (a). C_u, C_v plotted against non-dimensional time tf for EK10 and EK02. Solid lines correspond to C_u and dotted lines to C_v . (b). Nondimensional vertical gradient of mean streamwise velocity, $\Phi_M = \kappa z u_*^{-1} d \langle \bar{u} \rangle / dz$ plotted as a function of nondimensional height. Lines with markers +, o, □ correspond to $CHNL$, $EK10$ and $EK02$, respectively. The solid black line corresponds to the classical log law expected to hold in the surface layer.

lowest 10% of the boundary layer (Garra, 1992; Stoll and Porté-Agel, 2006). The values obtained from the simulations are consistent across the different levels of rotation and similar to values obtained previously using LES (Andren et al., 1994; Bou-Zeid et al., 2005; Stoll and Porté-Agel, 2006).

The normalized vertical shear stress profiles illustrate an important difference among the cases in Fig. 2. In a horizontally homogeneous velocity field under quasi-steady condition, the applied streamwise-pressure gradient balances the total-vertical stress gradient (e.g. Eqn. 1). As a result, a linear vertical profile of the horizontally averaged total stress ($\langle \bar{u}_1' \bar{u}_3' + \tau_{13} \rangle$) is expected for the $CHNL$ case that goes from a normalized values of -1 to a value of zero at the domain top (Fig. 2(a)). For the $EK02$ and $EK10$ cases, a linear total stress profile does not emerge because of a significant contribution to the stress profile from the spanwise stress component ($\langle \bar{u}_2' \bar{u}_3' + \tau_{23} \rangle$) that accounts for as much as 30% of the total stress at the ground level (Fig. 2(b)). The spanwise contribution is a result of the translation of momentum between the streamwise and spanwise directions by the Coriolis force (e.g. Eqn. 3).

Figure 3 shows the difference in rotational tendencies between $EK10$ and $EK02$ in terms of the vertical profile of the local Rossby number defined as $Ro_3 = \sqrt{\langle \omega_3^2 \rangle} / f$, where ω_3 denotes the surface-normal component of the vorticity vector. With increasing height from the ground, the influence of the Coriolis force grows larger which manifests in a decreasing ratio of inertia to Coriolis forces. $EK02$ clearly shows a greater degree of influence of Coriolis force at every height compared to $EK10$, which is consistent with the increased importance of spanwise stress component (Fig. 2).

Table 1 Simulation parameters and flow characteristics

	N_1, N_2	N_3	L_1, L_2 (Km)	L_3 (Km)	U_g (m/s)	δ (m)	Ro
$CHNL$	2048	64	128	1.5	0	1500.00	-
$EK10$	2048	64	128	1.5	10	1433.00	67
$EK02$	2048	64	128	0.75	2	550.69	33

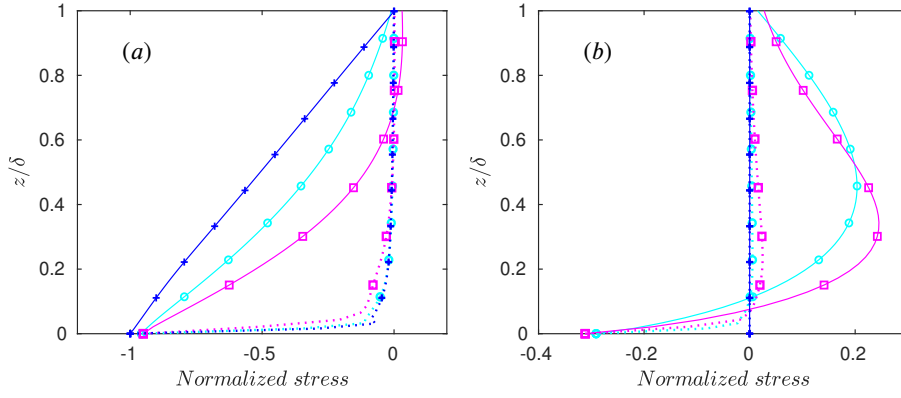


Fig. 2 Normalized vertical profiles of time and horizontally averaged resolved and SGS stresses. (a) $\langle \bar{u}_1' \bar{u}_3' + \tau_{13} \rangle$ and τ_{13} plotted as a function of height normalized by boundary layer height (δ) for cases *EK10*, *EK02* and *CHNL*. Solid lines correspond to $\langle \bar{u}_1' \bar{u}_3' + \tau_{13} \rangle$ and dotted lines correspond to τ_{13} . (b) $\langle \bar{u}_2' \bar{u}_3' + \tau_{23} \rangle$ and τ_{23} plotted as a function of normalized height for cases *EK10*, *EK02* and *CHNL*. Solid lines correspond to $\langle \bar{u}_2' \bar{u}_3' + \tau_{23} \rangle$ and dotted lines to τ_{23} . Line types $-o-$, $-\square-$ and $-+ -$ correspond to *EK10*, *EK02* and *CHNL*, respectively.

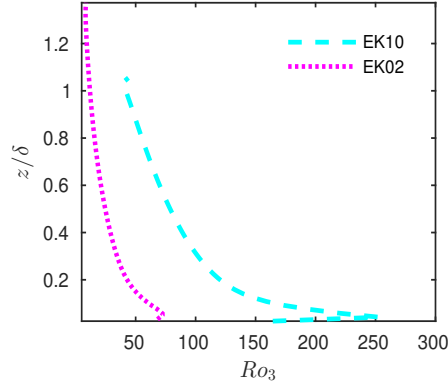


Fig. 3 Vertical Rossby number profile of *EK10* and *EK02* plotted as a function of normalized height.

3.2 Correlation and spectral characteristics

The resolved velocity fields contain a range of large active spatial length scales that are similar or greater to the boundary layer height. A common method used to estimate the extent of the large active scales in the flow is the autocorrelation function with one of its primary function being to define an integral length scale for a flow. By definition, VLMS are larger than the integral length scale but the autocorrelation function can still provide a relative measure of flow-length scales present in the three different cases. The panels on the left-hand side of Fig. 4 show the streamwise velocity correlation of the mid-boundary layer plane ($x_3^{ref} = \delta/2$) with all other discrete horizontal levels resolved in the simulations. The formal definition

of this correlation is

$$R_{uu}^{3d}(\Delta x_1, \Delta x_2, x_3, x_3^{ref}) = \frac{\langle u'(x_1, x_2, x_3^{ref}) u'(x_1 + \Delta x_1, x_2 + \Delta x_2, x_3) \rangle}{\langle u'^2(x_1, x_2, x_3^{ref}) \rangle}, \quad (5)$$

where, $\Delta x_1, \Delta x_2$ are spatial lags between the two points in x_1 - and x_2 -directions, respectively. Typically, juxtaposed low- and high-momentum streaks in the spanwise direction have been identified as a signature of the existence of VLSMs (Fang and Porté-Agel, 2015). For the *CHNL* case, iso-surfaces of both positive and negative correlation are visible where $R_{uu}^{3d} \geq 0.25$ is denoted by the red iso-surfaces and $R_{uu}^{3d} \leq -0.15$ is denoted by blue iso-surfaces. The *EK10* and *EK02* cases do not show negative correlation on either of the sides of the positively correlated regions for a value of $R_{uu}^{3d} \leq -0.15$. This is a first sign of the impact of rotation on characteristics of VLSMs. These plots also show the maximum vertical extent of influence of active scales existing in the mid-boundary layer. In *CHNL*, the influence of the largest active scales extends from the bottom of the domain up to 85% of the BL height. This was limited to 80% for the *EK10* and 70% for the *EK02* cases. The right-hand side panels of Fig. 4 show planar correlation of u_1 -velocity component at $z = 0.5\delta$ where, the planar autocorrelation is defined as:

$$R_{uu}^{2d}(\Delta x, \Delta x_2, x_3) = \frac{\langle u'(x_1, x_2, x_3) u'(x + \Delta x_1, x_2 + \Delta x_2, x_3) \rangle}{\langle u'^2(x_1, x_2, x_3) \rangle}. \quad (6)$$

The shape, orientation, and spread of the iso-lines are noticeably different for the three cases. Iso-lines of nominal correlation of 0.01 along with $-0.1, 0.1, 0.25$ are shown. Regions of negative correlation displayed by blue lines most prominently appear in the *CHNL* case. For the *EK10* case, very small regions of negative correlation are visible and for the *EK02* case regions of negative correlation do not appear alongside the large elongated positively correlated regions. The rotated orientation of the iso-lines in *EK10* and *EK02* indicate the presence of rotation in the flows while in the *CHNL* case the iso-lines are approximately aligned with x_1 and x_2 axes as expected for a mean-streamwise flow. A greater degree of rotation in *EK02* compared to *EK10* is also apparent from the orientation of the iso-lines corresponding to 0.1 and 0.01. The lines marked by nominal positive correlation of 0.01 infer that the uni-directional pressure gradient in a channel flow helps retain high coherence of the velocity field and the rotation in geostrophic flows substantially prohibits this coherence. This assessment can be quantified by the examining the integral length scales defined in the x_1 - and x_2 -directions as $L_{int,x_1} = \int_0^\infty dx R_{uu}^{2d}(x_1, 0)$ and $L_{int,x_2} = \int_0^\infty dy R_{uu}^{2d}(0, x_2)$, respectively. Here, a discrete version of the integral length scales were used (Träumner et al., 2015), where Δx_1^o and Δx_2^o indicate the location of zero crossings of the correlation function on the x_1 and x_2 axes, respectively.

$$L_{int,x_1} = \sum_{\Delta x_1=0}^{\Delta x_1^o} R_{uu}^{2d}(x_1 + \Delta x_1, 0, x_3) \Delta x_1 \text{ and} \quad (7)$$

$$L_{int,x_2} = \sum_{\Delta x_2=0}^{\Delta x_2^o} R_{uu}^{2d}(0, x_2 + \Delta x_2, x_3) \Delta x_2. \quad (8)$$

Equations 7 and 8 were evaluated at $x_3 = 0.25\delta$. Streamwise integral length scale of *CHNL* was determined to be 2569 m and that of *EK10* and *EK02* were, respectively, 877 m and

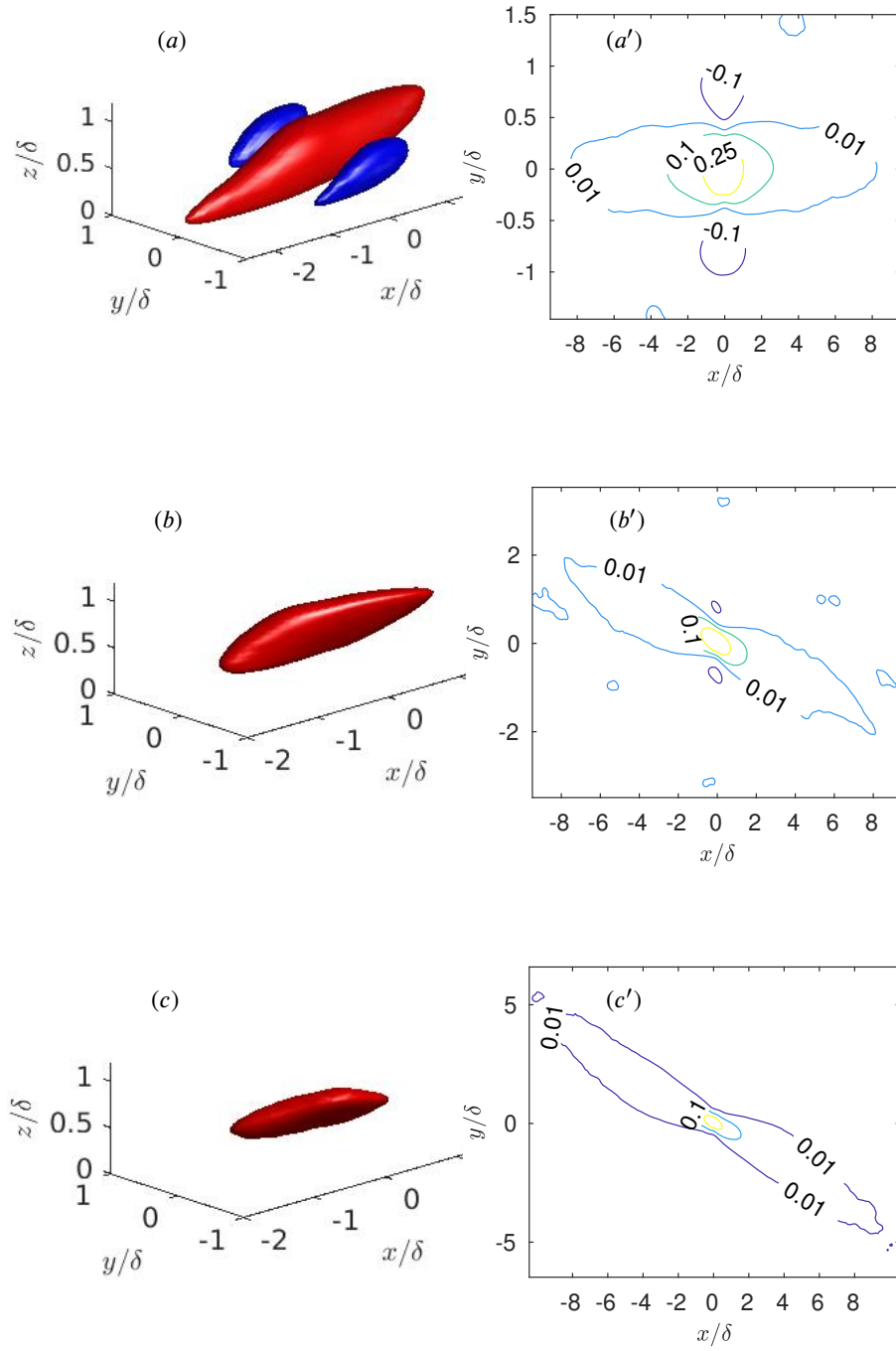


Fig. 4 Correlation of u -velocity component. (a), (b), (c) show correlation of reference level $z/\delta = 0.5$ with all other horizontal levels as defined by equation 5 for *CHNL*, *EK10*, and *EK02*, respectively. Red iso-surfaces denote correlation greater than or equal to 0.25 and blue iso-surfaces show negative correlation, smaller or equal to -0.15 . (a'), (b'), (c'). Show planar autocorrelation, R_{uu}^{2D} of *CHNL*, *EK10*, and *EK02* at $x_3 = 0.5\delta$, respectively.

265 *m*. Cross-stream integral length scales were, respectively, 382 *m*, 300 *m* and 160 *m* for
 251 the three cases.

252 In addition to velocity field correlations, velocity power spectral density is commonly
 253 used to examine the length-scale motions. Energy peak in the long-wavelength region or
 254 a plateau region in the long-wavelengths in the pre-multiplied spectra has been primarily
 255 used to identify VLSMs in channel flows (Fang and Porté-Agel, 2015; Guala et al., 2006). In
 256 Fig. 5 energy spectra of the horizontal velocity components premultiplied by the appropriate
 257 wavenumber and normalized by friction velocity are plotted as a function of the correspond-
 258 ing horizontal wavelength is normalized by δ . In the *CHNL* case (Fig. 5a), the typical high
 259 energy peak and plateau region for long wavelengths is clearly identifiable from the u_1 spec-
 260 tra confirming the existence of streamwise-aligned large scale structures along with VLSMs.
 261 The first peak or the beginning of the plateau, corresponds to LSMs and the second peak or
 262 the end of the plateau corresponds to VLSMs (Kim and Adrian, 1999). This plateau region
 263 with a slope of zero corresponds to the -1 slope production range expected for spectra that
 264 are not pre-multiplied (Perry et al., 1986; Saddoughi and Veeravalli, 1994). The same com-
 265 mon trend of decrease in turbulent energy with respect to distance from the wall is evident
 266 for all cases. It is noticeable in *CHNL* that for a height of 0.06δ the peak appears at the
 267 wavelength of 21δ whereas, at the height of 0.45δ the peak appears at 28δ . From the plotted
 268 lines it is observed that the high energy peaks corresponding to VLSMs shift towards larger
 269 wavelength up until a the height of $z/\delta = 0.3$. Also, an overall shrinking plateau region is
 270 observed as the distance from the surface increases. As the height increases the distinctive
 271 peak in the LSM region corresponding to a large amount of energy gradually ceases to ex-
 272 ist. This indicates that in the lower portion of the BL, LSMs contribute significantly to the
 273 total energy content. All these features conform to the findings of the previous studies that
 274 probed VLSM characteristics in channel flows. However, in the case of Ekman layer flows
 275 (Fig. 5(b), 5(c)) significantly different energy distributions are observed. Instead of bi-modal,
 276 skewed mono-modal distributions with or without a clear plateau region are produced. For
 277 the *CHNL* and *EK10* cases the highest energy peaks in the LSM regime shift towards the
 278 larger wavelengths with increasing distance from the wall. In contrast, for the *EK02* case
 279 the shift toward larger wavelengths is not as prominent and all of the peaks are concentrated
 280 within $\lambda_x/\delta = 1 \pm 0.2$. The observed difference in the length scales of the high energy con-
 281 taining motions between the Ekman layer cases i.e. *EK10* and *EK02* can be attributed to
 282 the difference in the magnitude of rotation present in the flows. Also, the spectral energy
 283 distributions in *EK02* are flatter than those of the *EK10* case while at the same time the rel-
 284 ative energy content of LSMs diminishes significantly. This could either mean the absence
 285 of VLSMs or that their contribution to the stream-wise energy is not as pronounced as in the
 286 other cases. The tails of the spectral energy distributions show significant difference between
 287 the three cases. The *CHNL* case has a sharp fall in the energy content of the small scale
 288 structures, while *EK10* has a gradual decline and *EK02* has a even slower decline. On the
 289 right hand side panels (*a'*), (*b'*), and (*c'*) show pre-multiplied and normalized u_2 -spectra with
 290 respect to spanwise wavelengths (λ_2) normalized by δ . The possibility of streamwise aligned
 291 large-scale structures being washed out due to the cross-stream velocity component can be
 292 inferred from u_2 -spectra. Intense energy in the cross stream scales would indicate such a pos-
 293 sibility. The energy distributions in the cross-stream scales in these cases are mono-modal
 294 with or without a clear plateau. The energy distributions the cross-stream velocity scales are
 295 similar between the different cases unlike the u_1 -spectra. The high-energy peaks move to-
 296 wards the larger wavelength region with increasing distance from the surface. *CHNL* and
 297 *EK10* show nearly similar distribution each with its most significant large scale being on
 298 the order of δ . At similar heights, similar length scales tend to have more energy in *EK10*

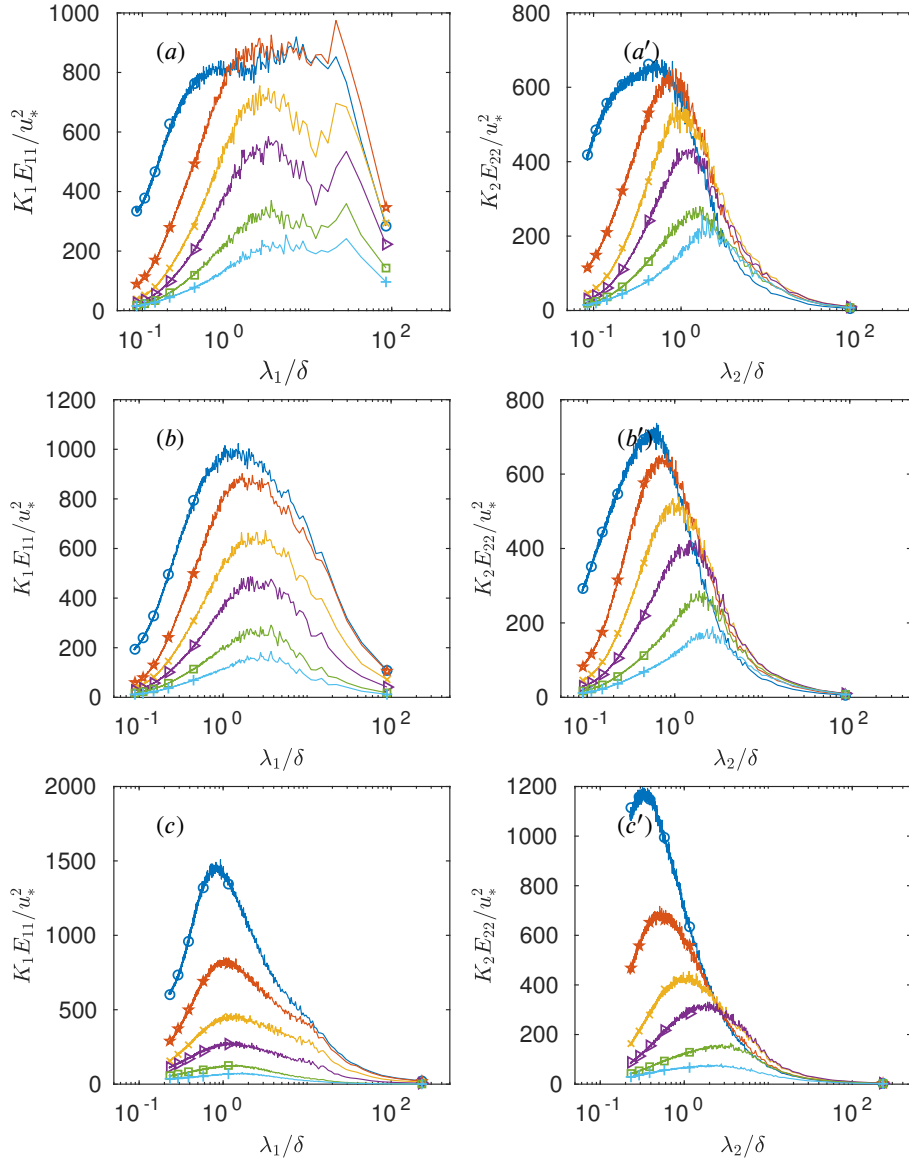


Fig. 5 Premultiplied velocity spectra against normalized wavelengths are shown for different cases. (a), (b), (c) show spectra of the u -component of the velocity for *CHNL*, *EK10* and *EK02*, respectively. (a'), (b') and (c') show spectra of the v -component of the velocity for *CHNL*, *EK10* and *EK02*, respectively. Curves marked with (\circ , \star , \times , ∇ , \square , $+$) correspond to heights $x_3/\delta = (0.06, 0.15, 0.30, 0.45, 0.71, 0.90) \pm 0.01$, respectively.

compared to *CHNL*. This is due to a higher magnitude in fluctuations of the u_2 velocity component. Energy content at each scale at each horizontal level is lower in *EK02* compared to *EK10* with a notable exception at $z = 0.054\delta$. These pre-multiplied spectra do not provide any conclusive evidence of the absence of VLSMs in Ekman layer flows although they do not show any evidence of the presence either. To address this issue in the next section alternative approaches are used to identify VLSMs that involve selective filtering and alternative VLSM definitions as well as quantifying the contributions of VLSMs to the surface shear stress.

Table 2 Fraction of the cumulative energy contained by all the spatial scales greater than the specified threshold at a height of $x_3 = 0.45\delta$ ($\pm 0.01\delta$) for the u_1 -component in the x_1 -direction

Threshold	δ	3δ	5δ	7δ	9δ	11δ
<i>CHNL</i>	0.841	0.633	0.524	0.461	0.416	0.383
<i>EK10</i>	0.771	0.490	0.356	0.278	0.227	0.190
<i>EK02</i>	0.693	0.396	0.283	0.220	0.178	0.146
Threshold	13δ	15δ	17δ	19δ	21δ	23δ
<i>CHNL</i>	0.359	0.339	0.320	0.305	0.290	0.277
<i>EK10</i>	0.167	0.147	0.130	0.116	0.105	0.096
<i>EK02</i>	0.122	0.105	0.090	0.079	0.070	0.064

3.3 Filtering and Conditional Averaging

Conditional averaging was carried out with a goal of further characterizing the size and shape of VLSMs and of identifying the contribution of VLSMs to shear stress, $\tau_{x,y} = \sqrt{\langle (u'_1 u'_3)^2 + (u'_2 u'_3)^2 \rangle}$, where, $u'_1 u'_2 = (u_1 - \langle u_1 \rangle_{x,y})(u_2 - \langle u_2 \rangle_{x,y})$, and $u'_2 u'_3 = (u_2 - \langle u_2 \rangle_{x,y})(u_3 - \langle u_3 \rangle_{x,y})$ with $\langle \rangle_{x,y}$ denoting the planar average. The conditional averaging was carried out at selected wall parallel planes to characterize the flows in the wall-normal direction and to have a quantitative account of coherent structures on horizontal planes. Many studies have examined the characteristics and contributions of coherent structures with length scales of order of δ or smaller (). Here, to facilitate the determination of contributions from only large scale coherent structures, smaller flow scales that fall within the inertial sub-range of turbulence were removed by filtering. Two-dimensional spectral cut-off filtering in the horizontal plane was used and the cut-off scale was selected as the distance of the selected surface from the ground. This filtering was designed to remove all horizontal scales smaller than the scales of the energy producing eddies. A new alternative definition of planar coherent structures was adopted to facilitate our analysis. Two-dimensional coherent structures were defined as the connected region of pixels either having negative u'_1 fluctuations (low momentum) or positive u'_1 fluctuations (high momentum). The adopted definition was motivated by the commonly reported presence of VLSMs in filtered velocity fields identified through visualization (Dennis and Nickels, 2011; Hutchins and Marusic, 2007). Visually, VLSMs appear to be long regions of low or high momentum fitting the definition assumed. Here, an objective analysis was devised using image-processing techniques to detect such long structures and quantify their spatial characteristics. In addition, to quantify the importance of a detected structure to momentum transport the ratio of shear stress fraction and area fraction was determined.

Here, horizontal transects of 3D structures were identified at different heights. To identify a 2D horizontal-transect of a structure a binary version of the velocity field was created. To identify low-momentum structures all positive streamwise velocity field fluctuations were set to zero and negative values were assigned a value of one so that on a given horizontal level

$$u'_1(x, y) = \begin{cases} 1, & u'_1 \leq 0 \\ 0, & u'_1 > 0. \end{cases} \quad (9)$$

Next the binary planar image was segmented and labeled using a connected component labeling technique Davies (2012). Spatial image moments and shape attributes for each labeled area were calculated including the centroid, area, major axis length, minor axis length, and orientation. The zeroth-order moment of a shape is the area of that shape. The ratio of first-order and zeroth-order moments yields the centroid of an image object. The major axis length is equivalent of the major axis length of an ellipse that has the same moments of inertia along the horizontal and vertical axes and also has the same moments of inertia along the principal axes. The orientation was measured as degrees of angle between the horizontal axis and the major axis of a shape. More details on spatial moments and discrete binary image shape attributes can be found in Pratt (2014). The major axis length of each labelled segment was and if it was greater than a specified threshold, the segment was marked as a possible horizontal transect through a VLSM. On these marked image objects ellipses with pre-determined major and minor axes lengths were drawn with coincident centroids. All such elliptical areas in five statistically independent frames were then averaged to characterize an average footprint of a VLSM. The frames were $L_{int,x}/U_c$ (sec) apart from each other in time where, the characteristic velocity U_c was taken as the mean velocity at the height of the BL. In the image segment identification process, an incremental range of length scales $(0.75n - 1.25n)\delta$ with $n = 2, 3, \dots, 24$ was used. Structures identified with in each range of scales on selected horizontal levels provided cumulative measurements of the contribution to the shear stress and turbulent kinetic energy by coherent structures on those 2D planes.

To quantify the importance and contribution of VLSMs to shear stress two quantities were calculated after averaging, the area fraction and the shear stress fraction. The total area fraction A_f , was calculated as,

$$A_f = \sum \frac{\mathbb{N}}{\mathbb{N}_a},$$

where \mathbb{N} represents the number of non-zero pixels within an individual ellipse and \mathbb{N}_a denotes the total number of pixels in the binary image. Summation over all area fractions yielded total area fraction. The total shear stress fraction $\tau_{x,y}^f$ was calculated as,

$$\tau_{x,y}^f = \frac{\sum \langle \tau_{x,y} \rangle \mathbb{N}}{\langle \tau_{x,y} \rangle_a \mathbb{N}_a},$$

where $\langle \tau_{x,y} \rangle_a$ is the average shear stress of the wall parallel plane and $\langle \tau_{x,y} \rangle$ is that of a selected elliptical area. An example of the determination process is presented in Fig. 6. The image on the left hand side shows a binarized image of the u'_1 field at the height of 0.15δ . The white regions represent negative u'_1 fluctuations and black regions represent positive velocity regions. In this picture all detected structures having lengths in the range of $\delta - 10\delta$ are shown as blue regions. On the right hand side, a two blue regions encircled with red ellipses and marked interior points painted in blue are shown. The detected regions were characterized with the major and minor axes lengths of the bounding ellipses and the painted blue points

were used as sampling points for calculating average shear stress. Finally, the ratio $\tau_{x,y}^f/A_f$ was studied to quantify the significance of the selected areas in terms of their contribution towards the shear stress. Figure 7 shows cumulative density functions of the lengths of

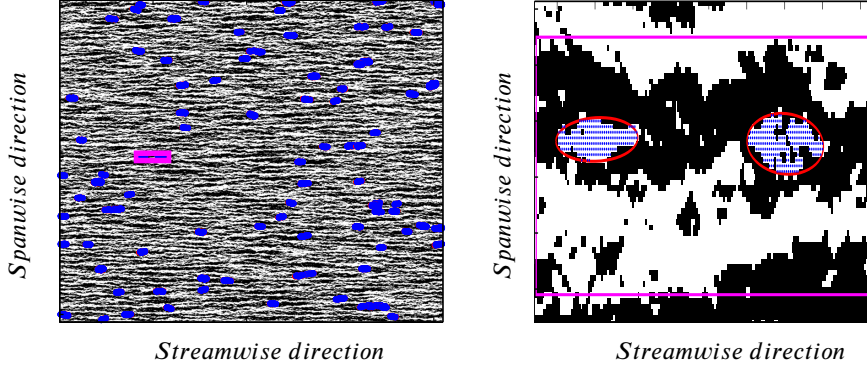


Fig. 6 (Left) For the *CHNL* case a cropped binarized negative u' velocity field image is shown which is overlaid with detected elliptical coherent structures with a range of major axis length lengths, $\delta - 10\delta$. (Right) Zoomed-in two detected structures with interior points painted in blue where average shear stresses were calculated are shown. Horizontal and vertical axes are aligned with streamwise and spanwise directions respectively

coherent structures as a function of height in the left panels along with the ratio $\tau_{x,y}^f/A_f$ in the right panels. The cumulative density functions highlight differences in the population of VLSMs existing in the u_1 -velocity fields. Between the three cases *CHNL* shows the presence of VLSM horizontal transects as large as 30δ on a surface-parallel plane at the height of 0.66δ and similar observation can be for *EK10* and *EK02*. However, a comparison of Figs. 7(a), (b) and (c) indicates that ratio of large-scale structures to small scale structures decreases for higher degrees of rotation in the velocity field. Also evident is the fact that the large-scale structures are scarce at lower levels i.e. in the surface layer but appear more frequently as the distance from the ground increases i.e. outer layers. In general the number of occurrences of large-scale structures is a function of height. To get a quantitative picture of the importance of such detected structures to horizontal shear stress, $\tau_{x,y}^f/A_f$ is plotted against normalized height in Fig. 7(d). Due to huge differences in the number of detected structures in each band, $\tau_{x,y}^f/A_f$ in Fig. 7(d), average major axis length in 7(e), and average minor axis length in 7(f) at each horizontal level were calculated as the expected values. The $\tau_{x,y}^f/A_f$ ratio plot shows the importance of the structures detected in terms of their contribution to overall shear stress at the respective horizontal levels. *CHNL* shows the highest contribution to shear stress from connected regions while *EK02* shows the minimum contribution. This Fig. also reveals a significant fact that structures or at least the VLSM horizontal transects on surface-parallel planes do not contribute significantly to shear stress in the surface layer. However, the authors refrain from drawing any strong conclusion from this result in the vicinity of the surface because of the use of a highly approximate modeled shear stress boundary condition in LES of the ABL. In general, as the distance from the bottom surface increases, the importance and contribution of these visually-identified long connected regions of low momentum increases gradually. The length scale of VLSMs likewise can also be observed to be a function of z in Fig. 7(e). Although, a slight difference in the maximum average length

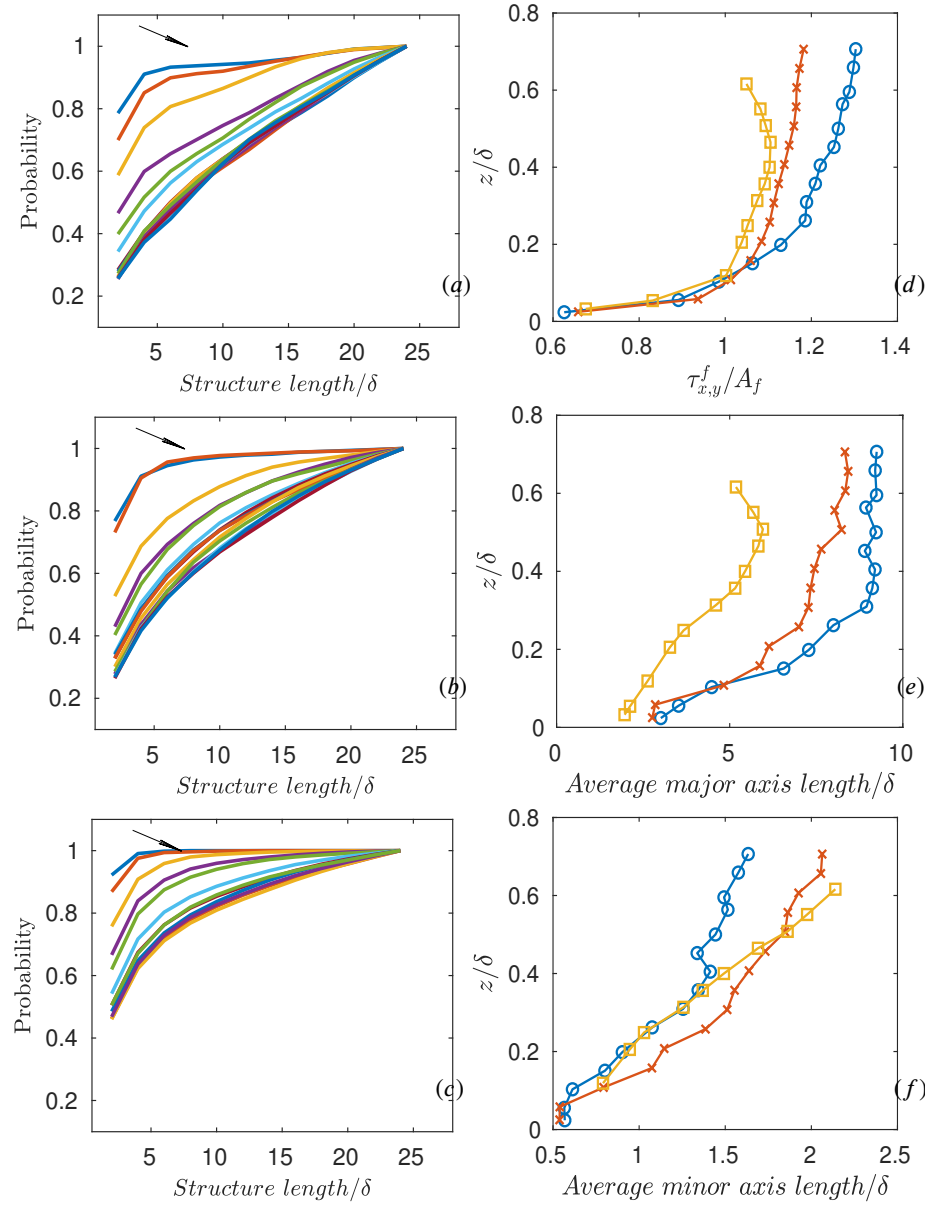


Fig. 7 Cumulative density function of coherent structure lengths, their aggregate contribution to shear stress as functions of height and their average lengths. The left panel shows cumulative density function of the structure lengths detected in the range $\delta - 25\delta$ for *CHNL* (a), *EK10* (b), and *EK02* (c) cases. The arrows point to the direction of increasing distance from the surface. The panel on the right hand side shows the ratio (d) $\tau_{x,y}^f/A_f$ plotted for different wall normal locations of all cases. (e) shows the mean length of major axes for all structures detected and (f) shows the mean minor axes lengths. Here (—○—) represents *CHNL*, (—×—) represents *EK10*, and (—□—) represents *EK02*.

of the structures is observed in *CHNL* and *EK10* cases i.e. 8.19δ at a height of 0.7δ for *CHNL* case and 8.4δ at a height of 0.65δ for *EK10* (fig. 7(e)), the trend in these two cases are almost identical. The shortest among the maximum average length appears in *EK02* as 5.95δ at a height of 0.5δ . As evident from the Fig. 7(f), the structure width increases with height consistently. At the highest measurement height *CHNL* shows the minimum structure width i.e. 1.47δ whereas, *EK10* and *EK02* show 2.06δ and 2.13δ , respectively. With the introduction of rotation in the velocity field the structures become shorter but wider.

A visual depiction of the 3D structure of the reported VLSMs as connected regions of low momentum fluid is shown in fig. 8. To determine the 3D structure the binarized u'_1 velocity field was examined for 2D horizontal transects on the horizontal plane at $2\Delta_z$ distance away from the ground where, Δ_z is the vertical grid spacing of the staggered grid. Upon identification of any connected region having a major axis length longer than a specified threshold, an enclosing 3D box was drawn centered at the centroid of the region. The 3D rectangular box extended from the bottom wall to the top of the simulation domain. The horizontal dimensions of the box in the streamwise and spanwise directions for the three different cases were estimated from the corresponding expected dimensions of the VLSMs (fig. 7(d) and 7(e)). The horizontal box dimensions were large enough to contain the VLSMs within the box and had streamwise lengths of 15δ , 15δ , 10δ and constant spanwise length of 2δ for *CHNL*, *EK10* and *EK02*, respectively. The conditional averaging revealed the average 3D shape of a VLSM which is expected from the very nature of the operation of conditional averaging. The fact that should be emphasized here is that the detection-condition was imposed only on a horizontal plane and no constraint was in place to the 3D shape or orientation. The assumption of similarity in size, orientation and shape of the structures around the selected averaging points is inherent to the idea of conditional averaging. If the assumptions hold true then a 3D coherent shape would appear. Considering these facts it can be inferred that the 3D structures obtained reveals a few characters of the VLSM. The conspicuous differences between VLSMs identified in each case appear in shape and dimension. For the *CHNL* case on an average VLSMs appear to have a symmetrical cylindrical shape in the middle which gets tapered off near the ends and the length in the mean wind direction is approximately 9δ . *EK10* case shows a structure which is slightly shorter in the mean wind direction and shows signs of rotation near the top where Ro is relatively low compared to that near the surface (see fig. 3). The average length can be identified to be approximately 7δ . For the *EK02* case a much shorter but wider structure is obtained. The effect of rotation in this case is the most prominent. The length can be identified to be approximately 5.7δ .

4 Conclusion

VLSMs were identified and their relative scales were compared for three different simulated flows. The simulation domain was large enough compared to the length scale of VLSMs not to impose any inhibition in the spatial development of these structures. One simulation provided the canonical channel flow case and the other two were Ekman layer simulations characterized by different degrees of rotation. Differences in the flow cases in terms of basic turbulent statistics along with the coherence were discussed. Coherence in the flows were compared in the light of correlation between different horizontal planes and integral length scales. The unidirectional constant pressure driven flow was observed to have the highest degree of coherence. The differences in coherence among the flow cases are reflected in the the determined mean length scales of the composite 3D structures of VLSMs.

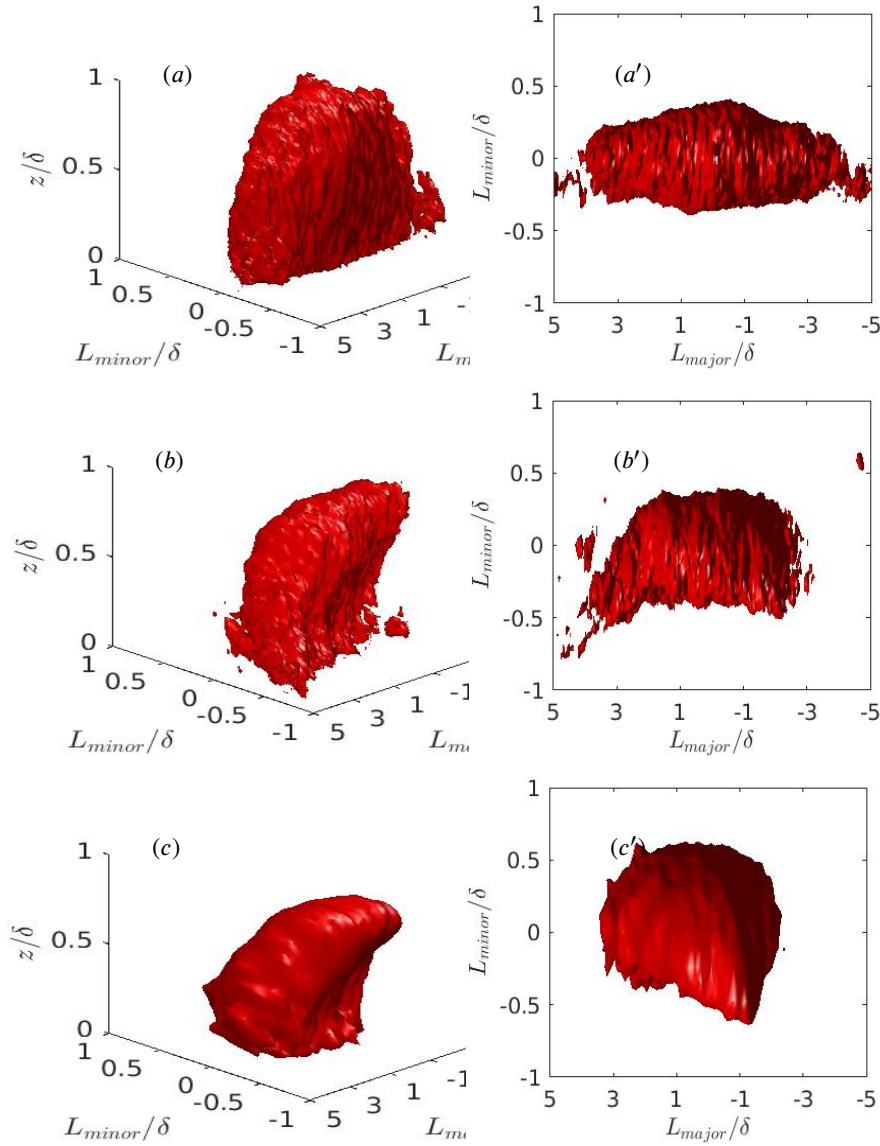


Fig. 8 (a), (b), (c) show the average 3D structures projected from detected 2D transects at the height of the first vertical grid point for the *CHNL*, *EK10* and *EK02* cases, respectively. (a'), (b'), (c') show the top view of the same 3D structures as shown on the left panels. Iso surfaces enclose values less than $\langle u \rangle - 1.5\sigma_u$

Previously, VLSMs were reported for flows only where rotation did not have any significant effect. Thus, the challenges of identification of VLSMs in rotational flows were not addressed. The most common problem in identification and detection of VLSMs is the lack of a concrete definition based upon which a detection algorithm could be developed. To address this issue and to test a hypothesis that VLSMs could be identified based on the reported visual characteristics of those structures i.e. as long streaks of low momentum fluid

primarily elongated in the streamwise direction, an alternative simple definition of VLSM was adopted. VLSMs were defined as the long connected regions of low momentum fluid. This definition yielded quantitatively consistent length scales of VLSMs with the same detected from pre-multiplied spectra for the *CHNL*. The detection of length scales of VLSMs from one dimensional pre-multiplied spectra quickly becomes marred as soon as rotation is introduced in the flow since, distinguishable dominant peaks ceases to appear. Adopting the alternative definition and utilizing the established image processing techniques lead to an effective technique of detection and measurement that work well even when rotation is introduced in the flow. This was verified by the identification of VLSMs in Ekman layer flows. A simple linear correspondence of the streamwise length scale was not observed with local Rossby number however, it was observed that in general rotation inhibits the streamwise length scale of the VLSMs but is conducive to the increase in length scale in the cross-stream direction. The greater the influence of rotation compared to inertial acceleration, the greater the cross-stream length scale is. It was also observed that irrespective of the forcing condition the length scale of the two dimensional planar structures were increasing in the direction normal to the ground. This result is consistent with the findings of de Silva et al. (2016).

References

- Andren A, Brown AR, Graf J, Mason PJ, Moeng C, Nieuwstadt FTM, Schumann U (1994) Large-Eddy Simulation of a Neutrally Stratified Boundary Layer: A Comparison of Four Computer Codes. *Q J R Meteorol Soc*
- Bailey BN, Stoll R (2013) Turbulence in sparse, organized vegetative canopies: A large-eddy simulation study. *Boundary-Layer Meteorology* 147(3):369–400, DOI 10.1007/s10546-012-9796-4
- Bailey BN, Stoll R (2016) The creation and evolution of coherent structures in plant canopy flows and their role in turbulent transport. *Journal of Fluid Mechanics* 789:425–460, DOI 10.1017/jfm.2015.749
- Bailey BN, Stoll R, Pardyjak ER, Mahaffee WF (2014) Effect of vegetative canopy architecture on vertical transport of massless particles. *Atmospheric Environment* 95:480 – 489, DOI <https://doi.org/10.1016/j.atmosenv.2014.06.058>
- Balakumar BJ, Adrian RJ (2007) Large and very-large-scale motions in channel and boundary-layer flows. *Philosophical Transactions of the Royal Society A*
- Baltzer JR, Adrian RJ, Wu X (2013) Structural organization of large and very large scales in turbulent pipe flow simulation. *Journal of Fluid Mechanics* 720
- Bou-Zeid E, Meneveau C, Parlange M (2005) A scale-dependent lagrangian dynamic model for large eddy simulation of complex turbulent flows. *Physics of Fluids* 17(2):025,105, DOI 10.1063/1.1839152, URL <https://doi.org/10.1063/1.1839152>
- Chung D, McKeon BJ (2010) Large-eddy simulation of large-scale structures in long channel flow. *Journal of Fluid Mechanics* 661
- Davies ER (2012) *Computer and machine vision : theory, algorithms, practicalities*. Elsevier/Academic Press
- Dennis DJC, Nickels TB (2011) Experimental measurement of large-scale three-dimensional structures in a turbulent boundary layer. part 2. long structures. *Journal of Fluid Mechanics* 673
- Esau IN (2003) The Coriolis effect on the coherent structures in the planetary boundary layers. *Journal of Turbulence* 4

- Fang J, Porté-Agel F (2015) Large-Eddy Simulation of Very Large-Scale Motions in the neutrally Stratified Atmospheric Boundary Layer. *Bound-Layer Meteorology* 155:397–416
- Fiedler H (1988) Coherent structures in turbulent flows. *Progress in Aerospace Sciences* 25(3)
- Ganapathisubramani B, Hutchins N, Monty JP, Chung D, Marusic I (2012) Amplitude and frequency modulation in wall turbulence. *Journal of Fluid Mechanics* 712
- Garrat JR (1992) The atmospheric boundary layer. Cambridge University Press
- Guala M, Hommema SE, Adrian RJ (2006) Large-scale and Very-large-scale motions in turbulent pipe flow. *Journal of Fluid Mechanics* 554:521–542
- Hossain M (1994) Reduction in the dimensionality of turbulence due to strong rotation. *Physics of Fluids* 6(3)
- Hussain AKMF (1986) Coherent structures and turbulence. *Journal of Fluid Mechanics* 173
- Hutchins N, Marusic I (2007) Evidence of Very Long Meandering Features in the Logarithmic Region of Turbulent Boundary Layers. *Journal of Fluid Mechanics* 579:1–28
- Jacob C, Anderson W (2017) Conditionally averaged large-scale motions in the neutral atmospheric boundary layer: Insights for aeolian processes. *Boundary-Layer Meteorology* 162(1):21–41, DOI 10.1007/s10546-016-0183-4, URL <https://doi.org/10.1007/s10546-016-0183-4>
- Kerhervé F, Roux S, Mathis R (2017) Combining time-resolved multi-point and spatially-resolved measurements for the recovering of very-large-scale motions in high Reynolds number turbulent boundary layer. *Experimental Thermal and Fluid Science*
- Kim KC, Adrian RJ (1999) Very large-scale motion in the outer layer. *Physics of fluids* 11:417–422, DOI 10.1063/1.869889
- Lee J, Lee JH, Choi JJ, Sung HJ (2014) Spatial organization of large- and very-large-scale motions in a turbulent channel flow. *Journal of Fluid Mechanics* 749:818–840
- Lee JH, Sung HJ (2011) Very-large-scale motions in a turbulent boundary layer. *Journal of Fluid Mechanics* 673:80–120
- Lewalle J, Delville J, Bonnet JP (2000) Decomposition of Mixing Layer Turbulence into Coherent Structures and Background Fluctuations. *Flow, Turbulence and Combustion* 64
- Miller NE, Stoll R (2013) Surface heterogeneity effects on regional-scale fluxes in the stable boundary layer: Aerodynamic roughness length transitions. *Boundary-Layer Meteorology* 149(2):277–301, DOI 10.1007/s10546-013-9839-5
- Monty JP, Stewart JA, Williams RC, Chong MS (2007) Large-scale features in turbulent pipe and channel flows. *Journal of Fluid Mechanics* 589
- Perry AE, Henbest S, Chong MS (1986) A theoretical and experimental study of wall turbulence. *Journal of Fluid Mechanics* 165:163–199
- Pratt WK (2014) Introduction to digital image processing. CRC Press, Taylor & Francis Group
- Saddoughi SG, Veeravalli SV (1994) Local isotropy in turbulent boundary layers at high Reynolds number. *Journal of Fluid Mechanics* 268:333–372, DOI 10.1017/S0022112094001370
- de Silva CM, Hutchins N, Marusic I (2016) Uniform momentum zones in turbulent boundary layers. *Journal of Fluid Mechanics*
- Stoll R, Porté-Agel F (2006) Dynamic subgrid-scale models for momentum and scalar fluxes in large-eddy simulation of neutrally stratified atmospheric boundary layers over heterogeneous terrain. *Water Resources Research* 42(1)

- 543 Stoll R, Porté-Agel F (2006) Effect of Roughness on surface boundary conditions for large-
544 eddy simulation. *Boundary-Layer Meteorology* 118:169–187
- 545 Stoll R, Porté-Agel F (2008) Large-eddy simulation of the stable atmospheric boundary
546 layer using dynamic models with different averaging schemes. *Boundary-Layer Me-*
547 *teorology* 126(1):1–28
- 548 Stoll R, Porté-Agel F (2009) Surface heterogeneity effects on regional-scale fluxes in sta-
549 ble boundary layers: Surface temperature transitions. *Journal of the Atmospheric Sci-*
550 *ences* 66(2):412–431, DOI 10.1175/2008JAS2668.1
- 551 Träumner K, Damian T, Stawiarski C, Wieser A (2015) Turbulent structures and coherence
552 in the atmospheric surface layer. *Bound-Layer Meteorology*
- 553 Yeung PK, Zhou Y (1998) Numerical study of rotating turbulence with external forcing.
554 *Physics of Fluids* 10(11)